

Journal of  
**Applied Remote Sensing**



## **Low-rank and sparse matrix decomposition-based anomaly detection for hyperspectral imagery**

Weiwei Sun

Chun Liu

Jialin Li

Yenming Mark Lai

Weiyue Li



# Low-rank and sparse matrix decomposition-based anomaly detection for hyperspectral imagery

Weiwei Sun,<sup>a,\*</sup> Chun Liu,<sup>b,c</sup> Jialin Li,<sup>a</sup> Yenming Mark Lai,<sup>d</sup> and Weiyue Li<sup>b</sup>

<sup>a</sup>Ningbo University, College of Architectural Engineering, Civil Engineering and Environment,  
818 Fenghua Road, Ningbo, Zhejiang 315211, China

<sup>b</sup>Tongji University, College of Surveying and Geo-informatics, 1239 Siping Road, Shanghai  
200092, China

<sup>c</sup>Key Laboratory of Advanced Engineering Survey of NASMG, 1239 Siping Road, Shanghai  
200092, China

<sup>d</sup>University of Maryland College Park, Applied Mathematics & Statistics, and Scientific  
Computation, Maryland 20742

**Abstract.** A low-rank and sparse matrix decomposition (LRaSMD) detector has been proposed to detect anomalies in hyperspectral imagery (HSI). The detector assumes background images are low-rank while anomalies are gross errors that are sparsely distributed throughout the image scene. By solving a constrained convex optimization problem, the LRaSMD detector separates the anomalies from the background. This protects the background model from corruption. An anomaly value for each pixel is calculated using the Euclidean distance, and anomalies are determined by thresholding the anomaly value. Four groups of experiments on three widely used HSI datasets are designed to completely analyze the performances of the new detector. Experimental results show that the LRaSMD detector outperforms the global Reed-Xiaoli (GRX), the orthogonal subspace projection-GRX, and the cluster-based detectors. Moreover, the results show that LRaSMD achieves equal or better detection performance than the local support vector data description detector within a shorter computational time. © 2014 Society of Photo-Optical Instrumentation Engineers (SPIE) [DOI: [10.1117/1.JRS.8.083641](https://doi.org/10.1117/1.JRS.8.083641)]

**Keywords:** anomaly detection; low-rank and sparse matrix decomposition; hyperspectral imagery; low-rank and sparse matrix decomposition detector.

Paper 13469 received Nov. 21, 2013; revised manuscript received Mar. 28, 2014; accepted for publication Apr. 1, 2014; published online May 1, 2014.

## 1 Introduction

Hyperspectral imagery (HSI) collects detailed spectral information of ground objects on the Earth's surface using hundreds of narrow and continuous bands.<sup>1</sup> With such an advantage over multispectral imagery, small and low-probability ground objects can then be accurately extracted using the methods of target detection or anomaly detection. The extraction results greatly benefit practical applications, including crop stress detection,<sup>2,3</sup> ecological monitoring,<sup>4,5</sup> invasive vegetation detection,<sup>6,7</sup> and military target detection.<sup>8,9</sup>

Compared with supervised target detection methods, anomaly detection methods do not require prior knowledge about targets; nor do they require data preprocessing, such as atmospheric compensation or spectral radiometric calibration.<sup>10,11</sup> The robustness of these methods has attracted the interest of researchers in the HSI field.<sup>12,13</sup> In anomaly detection, common ground objects that dominate the image scene are defined as the background, whereas small and low-probability ground objects that differ spectrally from the background are regarded as anomalies. Anomaly detection methods use the subtle spectral differences between ground objects to distinguish anomalies from the background.<sup>14,15</sup>

---

\*Address all correspondence to: Weiwei Sun, [nbsww@outlook.com](mailto:nbsww@outlook.com)

0091-3286/2014/\$25.00 © 2014 SPIE

A number of anomaly detection methods have yielded promising results. Reed and Yu proposed the Reed–Xiaoli (RX) detector, which is often used as the benchmark method for anomaly detection.<sup>16</sup> The RX detector has two modes: global and local. In the global mode, the background is derived from the full image scene, whereas in the local mode, the background is derived from the local neighborhood around the testing pixel. The RX detector assumes that the background pixels follow the uniform Gaussian distribution. It detects anomalies using the Mahalanobis distance, which incorporates the mean spectral vector of the background pixels along with their covariance matrix. Later, Kwon and Nasrabadi introduced the kernel-RX detector, a modified version of the RX detector that uses kernel functions.<sup>13</sup> The method improves detection performance by considering high-order nonlinear correlations between different bands of HSI data. Both the RX detector and its modified versions have been widely used in HSI data. However, the uniform Gaussian distribution assumption in the RX detector contradicts the reality of HSI data and fails to capture the complexity of HSI data.<sup>11,13</sup> Specifically, the local RX detector has a high false alarm rate for isolated objects.<sup>17</sup> Moreover, the inclusion of anomalies when modeling the background causes contaminated detection results.

To solve the above problems, global Gaussian mixture model (GGMM) methods, such as the Gaussian mixture model-generalized likelihood ratio test detector,<sup>15</sup> the cluster-based (CB) detector,<sup>18</sup> and the max-type detector,<sup>19</sup> were introduced. The GGMM methods assume that pixels within the same class have a uniform Gaussian distribution. Clusters are produced by unsupervised clustering and anomalies are detected by computing the Mahalanobis distance between each pixel and its nearest cluster. The GGMM approaches work well on complex image scenes having multiple classes and avoid poor detection results for isolated objects. However, their performance relies on clustering and, therefore, is unstable. Researchers also investigated linear mixture model (LMM) methods, such as the orthogonal subspace projection-RX (OSP-RX) detector<sup>20,21</sup> and the signal subspace processing detector,<sup>22</sup> to address the problems of the RX detectors. In LMM methods, each pixel is assumed to be a linear combination of endmember signatures with weights determined by the corresponding proportions (i.e., abundances). The LMM methods detect anomalies by projecting the HSI data onto a low-dimension subspace where the background components are suppressed. The determination of the optimum dimension of the subspace is then a crucial problem.

After GGMM and LMM methods were introduced, support vector (SV) approaches were proposed. SV approaches perform well in classification and are nonparametric. These approaches identify pixels that lie outside of the background support region as anomalies. Several detectors based on one-class classifiers were presented, including the local support vector data description (LSVDD) detector,<sup>10</sup> the Gaussian kernel-SVDD detector,<sup>11</sup> and the sparse kernel-based anomaly detector.<sup>23</sup> A common problem of SV methods is how to select an optimum kernel function.

Recently, multivariate outlier detection (MUD) methods, such as the projection pursuit detector,<sup>24</sup> the blocked adaptive computationally efficient outlier nominator detector, and the minimum covariance determinant detector,<sup>25</sup> have been introduced. These MUD methods regard the anomaly detection problem as outlier detection in a projected space of the HSI data. However, the convergence of object functions used for projection is sensitive to initial conditions.<sup>26</sup>

Manifold learning (ML) techniques, such as the robust locally linear embedding detector<sup>27</sup> and the local tangent space alignment detector,<sup>28</sup> were also proposed for anomaly detection. The ML detectors identify points that lie far away from the main manifolds in the embeddings as anomalies. Detection results depend on the parameters of neighborhood size and embedding dimension.

This paper proposes the low-rank and sparse matrix decomposition (LRaSMD) method to detect anomalies in HSI data. The LRaSMD detector is inspired by the idea that a matrix can be separated as the sum of a low-rank matrix and a sparse matrix. Although prior work on LRaSMD has already been done,<sup>29–32</sup> our study makes the contribution of applying LRaSMD to the problem of anomaly detection in HSI data. The new detector assumes the background images of HSI data are low-rank and the anomalies are spatially sparse in the image scene of each band. It then aims to separate the anomalies from the background. The LRaSMD detector features three main advantages. First, the new detector separates anomalies from the background in one step. Current detectors have to first model the background with statistical or geometric methods and then

distinguish the anomalies from the background. In contrast, the new detector separates the anomalies from the background in one step by solving a constrained convex optimization problem. Second, the LRaSMD detector avoids the negative effects of including anomalies in the background model. Traditional methods include anomalies when modeling the background. The background model is then corrupted, and the detection result is degraded. Consider the RX method for example. The method can be thought of as the inverse process of principal component analysis (PCA). It tries to find small-sized and low-probability anomalies that exist in the minor components.<sup>33</sup> A single grossly corrupted observation in the HSI data can cause the estimated principal components to be far away from the true ones and seriously contaminate the background model.<sup>34</sup> In contrast, the LRaSMD detector avoids this problem by separating anomalies from the background in one step. Third, the LRaSMD detector has a lower computational complexity than traditional methods and, therefore, is more practical for realistic applications in detecting anomalies.

The rest of the paper is organized as follows. Section 2 explains the LRaSMD method for HSI data. Section 3 analyzes the performances of the LRaSMD method using four groups of experiments on three widely used realistic HSI datasets. Section 4 states conclusions and outlines future work.

## 2 LRaSMD Method for HSI Data

In this section, the LRaSMD detector for HSI data is proposed. First, the modeling of background and anomalies in the LRaSMD detector is described. Next, the recovery method of the background and anomaly matrices is explained. After that, the approach of detecting anomalies with the sparse anomaly matrix is reported, and finally, the new method is summarized.

### 2.1 Modeling of Background and Anomalies

In a single-band image from HSI data, the background is modeled as continuous and smooth. It reflects the overall spectral characteristics of ground objects in the image scene. In contrast, anomalies are modeled as low-probability spectral responses that significantly deviate from the background measurements. Accordingly, the spectral response of each pixel  $x_i$  in the  $m$ 'th band image can be decomposed as Eq. (1).

$$x_i^m = b_i^m + s_i^m \quad \text{and} \quad \begin{cases} s_i^m = 0, & \text{if } x_i \text{ belongs to the background} \\ s_i^m \neq 0, & \text{if } x_i \text{ belongs to anomalies} \end{cases}, \quad (1)$$

where  $b_i^m$  is the background component of each pixel, and  $s_i^m$  is the corresponding anomaly component. If  $x_i^m$  belongs to the background, the anomaly component  $s_i^m$  equals zero; otherwise,  $s_i^m$  is nonzero. The initial image is then decomposed as the sum of the background component (i.e., the background image) and the anomaly component (i.e., the anomaly image), as shown in Fig. 1. The anomaly image is sparse, containing few nonzero entries, and reflects the locations of the anomalies in the image.

For hyperspectral images, the spectral vector  $X_i \in R^D$  of each pixel  $x_i$  can be decomposed as the sum of the background component and the anomaly component, as illustrated in Eq. (2).

$$\underset{1 \times D}{X_i} = \underset{1 \times D}{B_i} + \underset{1 \times D}{S_i}, \quad (2)$$

where  $B_i = [b_i^1, \dots, b_i^m, \dots, b_i^D]$ ; and  $S_i = [s_i^1, \dots, s_i^m, \dots, s_i^D]$ ; are the background and anomaly components of the spectral vector  $X_i$ , respectively. The anomaly component  $S_i$  records the anomaly features of pixel  $x_i$  against the background for each single-band image. Each entry in  $S_i$  may be either zero or nonzero since different spectral features among different bands may cause pixel  $x_i$  to be background at a certain spectrum and an anomaly in another.

If we stack all the spectral vectors into the real HSI dataset  $\tilde{X} = [X_1, X_2, \dots, X_N]^T \in R^{N \times D}$ , where  $N$  and  $D$  stand for the number of pixels and bands, respectively, the matrix  $\tilde{X}$  can be decomposed as Eq. (3).

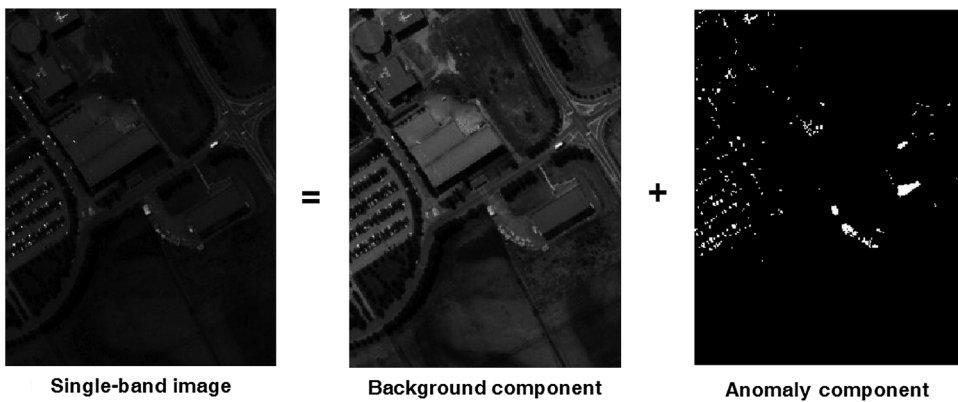


**Fig. 1** The background component and anomaly component of a single-band image.

$$\tilde{\mathbf{X}}_{N \times D} = \tilde{\mathbf{B}}_{N \times D} + \tilde{\mathbf{S}}_{N \times D}, \quad (3)$$

where  $\tilde{\mathbf{B}} = [\mathbf{B}_1, \mathbf{B}_2, \dots, \mathbf{B}_N]^T$  is the background matrix, with each row representing the background component of a spectral vector, and  $\tilde{\mathbf{S}} = [\mathbf{S}_1, \mathbf{S}_2, \dots, \mathbf{S}_N]^T$  is the anomaly matrix, with each row representing the anomaly component of a spectral vector. Each column of  $\tilde{\mathbf{B}}$  and  $\tilde{\mathbf{S}}$  stands for the background and anomaly components of a single-band image at a certain spectrum, respectively. In summary, the matrix  $\tilde{\mathbf{B}}$  represents the background information of HSI data, and the matrix  $\tilde{\mathbf{S}}$  represents the anomaly information.

In real-world HSI data, the entries in a spectral vector are corrupted with noise caused by precision limits of the imaging spectrometer and errors in analog to digital conversion. The noise can usually be modeled as identically and independently distributed (i.e., i.i.d.) Gaussian random variables. The Gaussian assumption is used mainly because of its mathematical tractability in the detection model. Equation (3) can then be transformed to Eq. (4).

$$\tilde{\mathbf{X}}_{N \times D} = \tilde{\mathbf{B}}_{N \times D} + \tilde{\mathbf{S}}_{N \times D} + \tilde{\mathbf{N}}_{N \times D}, \quad (4)$$

where  $\tilde{\mathbf{N}}$  is the noise matrix whose entries are i.i.d. Gaussian random variables. Since the matrix  $\tilde{\mathbf{B}}$  represents the background components, the matrix is nonsparse. Due to strong intraband correlations, each spectral vector can be expressed as the linear combination of several basis vectors (i.e., endmembers). The background matrix  $\tilde{\mathbf{B}}$  is assumed to lie on a certain low-dimension subspace, having low-rank properties,<sup>35,36</sup> since the background consists of almost all the information from the HSI data. On the other hand, anomalies are assumed to be distributed randomly with low probability, that is, nonzero entries in  $\tilde{\mathbf{S}}$  are sparse and scattered uniformly at random. Therefore, if we can reconstruct both the low-rank matrix and the sparse matrix of Eq. (4), the low-rank matrix will capture the global background information, while the sparse matrix will contain the anomalies. The sparse matrix can then be used to detect anomalies in the HSI data.

## 2.2 Recovery of Background and Anomaly Components

In Eq. (4), the ranks of the column and row space of  $\tilde{\mathbf{B}}$  are unknown. Furthermore, the number and locations of sparse components in  $\tilde{\mathbf{S}}$  are unknown. Hence, the problem in Eq. (4) is unsolvable by traditional methods because the number of unknown components exceeds the number of measurements of  $\tilde{\mathbf{X}}$ . Fortunately, convex optimization methods have been proposed to recover exactly both the low-rank matrix  $\tilde{\mathbf{B}}$  and the sparse matrix  $\tilde{\mathbf{S}}$ . In other works,<sup>37,38</sup> the problem in Eq. (4) has been transformed into a relaxed robust principal component pursuit problem. The objective function combines nuclear norm minimization and  $L_1$ -norm minimization, and the accelerated proximal gradient (APG) algorithm solves the problem. However, the recovery results of the APG algorithm strongly depend on the design of continuation schemes, and the regular generic continuation in the algorithm does not guarantee sufficient accuracy or convergence in practical applications.<sup>34</sup>

In this paper, we use the Go Decomposition (GoDec) algorithm to solve the problem in Eq. (4).<sup>39</sup> The algorithm controls the model complexity of the reconstruction by restricting both the rank of the background matrix  $\tilde{\mathbf{B}}$  and the cardinality (i.e., the sparsity level) of the anomaly matrix  $\tilde{\mathbf{S}}$ . It works by minimizing the decomposition error (i.e., the Frobenius norm of noise) in Eq. (5).

$$\arg \min_{\tilde{\mathbf{B}}, \tilde{\mathbf{S}}} \|\tilde{\mathbf{X}} - \tilde{\mathbf{B}} - \tilde{\mathbf{S}}\|_F^2 \quad \text{subject to } \text{rank}(\tilde{\mathbf{B}}) \leq r \quad \text{and} \quad \text{card}(\tilde{\mathbf{S}}) \leq kN, \quad (5)$$

where  $\|\cdot\|$  represents the Frobenius norm, and  $r$  and  $k$  are the restrictions on the rank of  $\tilde{\mathbf{B}}$  and the sparsity level of  $\tilde{\mathbf{S}}$ , respectively. The rank  $r$  controls the information of the background matrix  $\tilde{\mathbf{B}}$  taken from HSI data, and the sparsity level  $k$  of  $\tilde{\mathbf{S}}$  reflects the ratio of the anomalies in the image scene. The decomposition error monotonically decreases as iterations increase. Hence, the problem in Eq. (5) can be transformed into the following two subproblems.

$$\begin{cases} \tilde{\mathbf{B}}_t = \arg \min_{\text{rank}(\tilde{\mathbf{B}}) \leq r} \|\tilde{\mathbf{X}} - \tilde{\mathbf{B}} - \tilde{\mathbf{S}}_{t-1}\|_F^2 \\ \tilde{\mathbf{S}}_t = \arg \min_{\text{card}(\tilde{\mathbf{S}}) \leq k} \|\tilde{\mathbf{X}} - \tilde{\mathbf{B}}_t - \tilde{\mathbf{S}}\|_F^2 \end{cases}, \quad (6)$$

where  $\tilde{\mathbf{B}}_t$  and  $\tilde{\mathbf{S}}_t$  are optimization results at the  $t$ 'th iteration. Initially, the iteration time  $t$  is set as  $t = 0$ ,  $\mathbf{B}_t$  is set to be  $\tilde{\mathbf{X}}$ , and  $\mathbf{S}_t$  is set to be a zero matrix. In each iteration, the updating of  $\mathbf{B}_t$  is achieved by singular value hard thresholding<sup>40</sup> using  $\tilde{\mathbf{X}} - \mathbf{S}_{t-1}$ , and the updating of  $\mathbf{S}_t$  is obtained by the entry-wise hard thresholding of  $\tilde{\mathbf{X}} - \mathbf{B}_t$ .

$$\begin{cases} \mathbf{B}_t = \sum_{i=1}^r \lambda_i \mathbf{U}_i \mathbf{V}_i^T, \text{SVD}(\tilde{\mathbf{X}} - \mathbf{S}_{t-1}) = \mathbf{U} \Lambda \mathbf{V}^T \\ \mathbf{S}_t = \mathbf{P}_\Omega(\tilde{\mathbf{X}} - \mathbf{B}_t), \Omega : |(\tilde{\mathbf{X}} - \mathbf{B}_t)_{i,j} \in \Omega| \neq 0 \quad \text{and} \quad \geq |(\tilde{\mathbf{X}} - \mathbf{B}_t)_{i,j} \in \bar{\Omega}|, \quad |\Omega| \leq k, \quad \bar{\Omega} = \text{supp}(\mathbf{S}_{t-1}) \end{cases}, \quad (7)$$

where SVD is the singular value decomposition,  $\lambda_i$  is the  $i$ 'th largest singular value of  $\tilde{\mathbf{X}} - \mathbf{S}_{t-1}$ ,  $\Omega$  is the nonzero subset of first  $k$  largest entries of  $\|(\tilde{\mathbf{X}} - \mathbf{B}_t)\|$ ;  $\mathbf{P}_\Omega(\cdot)$  is the projection of a matrix to the entry set  $\Omega$ , and  $\bar{\Omega}$  is the support (i.e., the nonzero entry set) of matrix  $\mathbf{S}_{t-1}$ . The bilateral random projection<sup>41</sup> and the modification of power scheme<sup>42</sup> are used to increase the computational speed of SVD of  $\tilde{\mathbf{X}} - \mathbf{S}_{t-1}$  using approximations. The GoDec algorithm terminates when the decomposition error  $\|\tilde{\mathbf{X}} - \tilde{\mathbf{B}}_t - \tilde{\mathbf{S}}_t\|_F^2$  converges to a local minimum. The local optimum of the low-rank background matrix  $\tilde{\mathbf{B}}$ , the sparse anomaly matrix  $\tilde{\mathbf{S}}$ , and the noise matrix  $\tilde{\mathbf{N}}$  are then achieved.

### 2.3 Detection of Anomalies with the Sparse Anomaly Matrix

With the above recovery process, the anomaly matrix  $\tilde{\mathbf{S}}$  is separated from the background matrix  $\tilde{\mathbf{B}}$  and the noise matrix  $\tilde{\mathbf{N}}$ . In the matrix  $\tilde{\mathbf{S}}$ , each row vector  $\mathbf{S}_i = [s_i^1, \dots, s_i^m, \dots, s_i^D]$ ; corresponds to the anomaly components of spectral response for each pixel  $x_i$  against the background. Hence, the matrix  $\tilde{\mathbf{S}}$  can be used to detect the anomalies in HSI data. The anomalies are assumed to be spatially scattered at random in the image scene, and therefore, the anomaly components of the row vectors of  $\tilde{\mathbf{S}}$  are independent and uncorrelated. Consider the anomaly matrix as the real vector sets  $\tilde{\mathbf{S}} = [\mathbf{S}_1, \mathbf{S}_2, \dots, \mathbf{S}_N]^T$ ; the Euclidean distance is utilized to calculate the anomaly value for each pixel. The Euclidean distance rather than the Mahalanobis distance is implemented in the new approach because of uncorrelations among row vectors in matrix  $\tilde{\mathbf{S}}$ . The anomaly value  $d_i$  for pixel  $x_i$  is obtained via Eq. (8).

$$d_i = \sqrt{(\mathbf{S}_i - \bar{\mathbf{S}})(\mathbf{S}_i - \bar{\mathbf{S}})^T}, \quad (8)$$

where  $\mathbf{S}_i$  is the anomaly component of spectral vector for pixel  $x_i$  (i.e., the  $i$ 'th row in  $\tilde{\mathbf{S}}$ ), and  $\bar{\mathbf{S}}$  is the mean row vector of the sparse matrix  $\tilde{\mathbf{S}}$ . A larger anomaly value indicates that the pixel belongs to an anomaly with higher probability. Pixels in the image with an anomaly value above a manually selected threshold  $\eta$  are determined to be anomalies.

## 2.4 Summary of the LRaSMD Method

The LRaSMD detector for HSI data relies on the idea of matrix decomposition and separates the anomaly information from the background information in one step using constrained convex optimization. The method consists of the following steps:

1. Hyperspectral images are transformed from a cube into a two-dimensionsl real matrix  $\tilde{X}$ .
2. After setting the parameters of rank  $r$  and the sparsity level  $k$ , the GoDec algorithm optimizes the problem in Eq. (5). The low-rank background matrix  $\tilde{B}$ , the sparse anomaly matrix  $\tilde{S}$ , and the noise matrix  $\tilde{N}$  in Eq. (4) are obtained.
3. Anomaly values for all pixels are calculated with the Euclidean distance using row vectors of the sparse matrix  $\tilde{S}$  in Eq. (8).
4. Pixels are determined to be anomalies if their anomaly values exceed the threshold parameter  $\eta$ .

The computational complexity of GoDec algorithm in each iteration is less than  $O[r(r^2 + 2Nr + 4N)]$ ,<sup>39</sup> the calculation of the Euclidean distance requires  $O(ND^2)$ , and the complexity of locating the anomalies is  $O(N)$ . Therefore, the total complexity of the LRaSMD detector requires  $O[N(D^2 + 2Tr^2 + 4Tr + 1) + Tr^3]$ , where  $N$  and  $D$  are the number of pixels and bands in HSI data,  $r$  is the rank of the background matrix with  $r \ll D$ , and  $T$  is the number of iteration steps. Table 1 compares the computational complexity of the LRaSMD detector with four widely used detectors: global Reed-Xiaoli (GRX), OSP-GRX, CB, and LSVDD. For the OSP-GRX detector, the SVD algorithm of the correlation matrix of HSI data is used to construct the projected subspace,<sup>43</sup> where  $P$  is the dimension of the projected subspace. In the CB detector, we use the  $k$ -means algorithm to cluster the HSI data.<sup>44</sup>  $Q$  is the number of iteration steps, and  $C$  is the number of clusters. In the LSVDD detector, we use the Gaussian radial basis function (RBF) kernel,<sup>10</sup> and  $M$  is the number of training pixels in the hollow background window. We observe that the LRaSMD has a lower computational complexity among all five detection algorithms.

## 3 Experimental Results and Discussion

In this section, we investigate the performances of the LRaSMD detector using four groups of experiments on three realistic HSI datasets.

### 3.1 Description of HSI Datasets

The Pavia Center (PaviaC) dataset was downloaded from the Computational Intelligence Group of the Basque Country University and is available at [http://www.ehu.es/ccwintco/index.php/Hyperspectral\\_Remote\\_Sensing\\_Scenes](http://www.ehu.es/ccwintco/index.php/Hyperspectral_Remote_Sensing_Scenes). The dataset was acquired by the reflective optics system imaging spectrometer (ROSIS) sensor and has been widely used in many applications.<sup>45–47</sup> The dataset covers the Pavia Center in northern Italy and has accurate ground truth information. The number of bands in the initial dataset is 115 with 1.3-m spatial resolution covering the spectral range from 430 to 860 nm. In the experiment, a smaller subset is segmented from the initial larger image. The subset contains 115 × 120 pixels and 102 bands after removing

**Table 1** The contrast in computational complexity of different detectors.

Computational complexity of detectors				
LRaSMD	GRX	OSP-GRX	CB	LSVDD
$O[N(D^2 + 2Tr^2 + 4Tr + 1) + Tr^3]$	$O[N(2D^2 + 1) + D^3]$	$O[N^2(N + 1) + N(D^2 + 2P^2 + 1) + P^3]$	$O[N(QDC + D^2 + 1)]$	$O(NM^3)$

Note: LRaSMD, low-rank and sparse matrix decomposition; GRX, global Reed-Xiaoli; OSP, orthogonal subspace projection; CB, cluster based; LSVDD, local support vector data description.

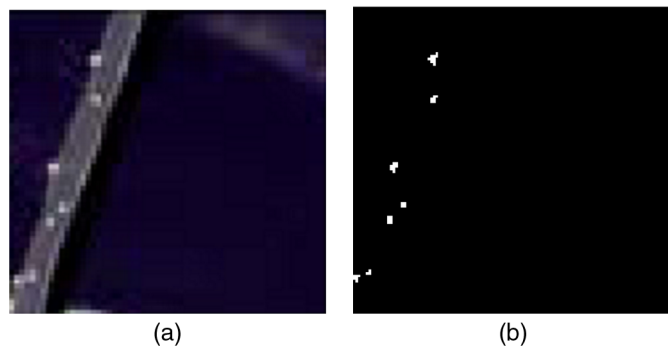


**Fig. 2** (a) The false-color image (bands 68, 30, and 2) and (b) the ground truth of anomalies in PaviaC dataset.

low signal-to-noise ratio (SNR) bands. In the false-color image of Fig. 2(a), three ground objects constitute the background: bridge, water, and shadows. Anomaly pixels representing vehicles on the bridge and the bare soil near the bridge pier also appear in the image scene. The ground truth of the anomalies is shown in Fig. 2(b). The number of anomaly pixels is 64 and the information of anomalies is listed in Table 2.

The Botswana dataset was downloaded from the Remote Sensing Group of the University of Texas at Austin and is available at <http://www.csr.utexas.edu/hyperspectral/index.html>. The dataset consists of NASA EO-1 satellite imagery collected by the Hyperion sensor over the area of Okavango Delta, Botswana. The dataset was acquired on May 31, 2001, with 30-m spatial resolution and 10-nm spectral resolution, covering the spectrum within 400 to 2500 nm. The pre-processing work was performed by the UT Center for Space Research to mitigate the effects of bad detectors, interdetector miscalibration, intermittent anomalies, and water absorption, leaving 145 bands as candidate features: [10 to 55, 82 to 97, 102 to 119, 134 to 164, 187 to 220]. The false color image shown in Fig. 3(a) is a smaller subset of the larger dataset. It contains 235 × 255 pixels and consists of ground observations from four identified classes: woodlands, savanna, floodplain, and mopane.<sup>48,49</sup> These classes are identified to reflect the impact of flooding on vegetation in the study area. In the image scene, 35 pixels were selected as anomalies, as shown in Fig. 3(b), since they are spectrally different from the main ground objects. According to their different background, the anomalies can be classified into three groups, as illustrated in Table 2. Anomaly1 represents anomaly pixels in the background of woodlands and mopane. Anomaly2 represents anomaly pixels in the background of woodlands and savanna. Anomaly3 represents anomaly pixels in the background of woodlands, savanna, and floodplain.

The PaviaU dataset achieved from the ROSIS sensor was also downloaded from the website of the Computational Intelligence Group of the Basque Country University. The dataset covers the area of Pavia University in northern Italy and contains 1096 × 1096 pixels in the image scene using 102 bands. A smaller dataset shown in Fig. 4(a) was segmented from the larger image. It contained 310 × 235 pixels and 99 bands after removing low-SNR bands. In the figure, six main

**Table 2** The information of anomalies in different backgrounds.

Datasets	Anomaly group	Number of pixels	Main ground objects of background
PaviaC	Anomaly	64	Bridge, water, and shadows
Botswana	Anomaly1	18	Woodlands and mopane
	Anomaly2	10	Woodlands and savanna
	Anomaly3	7	Woodlands, savanna, and floodplain
PaviaU	Anomaly1	308	Asphalt, gravel, trees, self-blocking bricks, and shadows
	Anomaly2	168	Asphalt, meadow, trees, and shadows

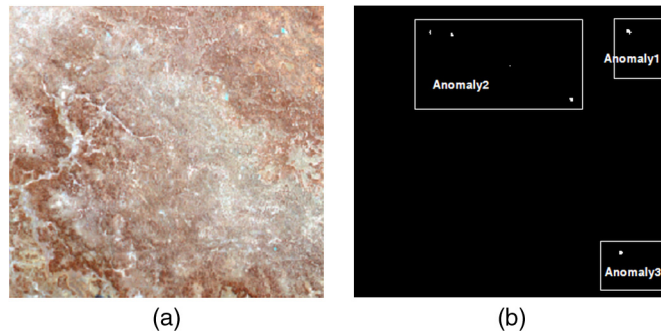


**Fig. 3** (a) The false-color image (bands 50, 27, and 17) and (b) the ground truth of anomalies in Botswana dataset.

ground objects constitute the background: asphalt, meadow, gravel, trees, self-blocking bricks, and shadows. Pixels representing different vehicles in the image scene were regarded as anomalies because they are spectrally different from the main ground. According to different background, the 476 pixels of anomalies can be classified into two groups, as illustrated in Table 2. Anomaly1 represents anomaly pixels in the background of asphalt, gravel, trees, self-blocking bricks, and shadows. Anomaly2 represents anomalies in the background of asphalts, meadow, trees, and shadows. The ground truth of the anomaly pixels is shown in Fig. 4(b).

### 3.2 Experimental Results

We conduct four groups of experiments using the PaviaC, Botswana, and PaviaU datasets described above in order to completely analyze the performances of our LRaSMD detector. First, we explore the separability performance of the LRaSMD detector in distinguishing the anomalies from the background and compare the results with those of the GRX, OSP-GRX, and CB detectors. Second, we analyze the effects from the changing rank of background matrix on the performance sensitivity of the LRaSMD detector. Third, we investigate the effects from the changing sparsity level of the anomaly matrix on the performance sensitivity of the new detector. Finally, we make holistic comparisons in detection performance between the LRaSMD and other four state-of-the-art detectors, including the GRX, OSP-GRX, CB, and LSVDD detectors. In the experiments, the receiver operating characteristic (ROC) curve that depicts both the probability of detection and the probability of false alarm rate is utilized to fully evaluate the detection performance of all detectors. For the OSP-GRX detector, the SVD decomposition is utilized to construct the projected subspace. The clustering approach in the CB detector is

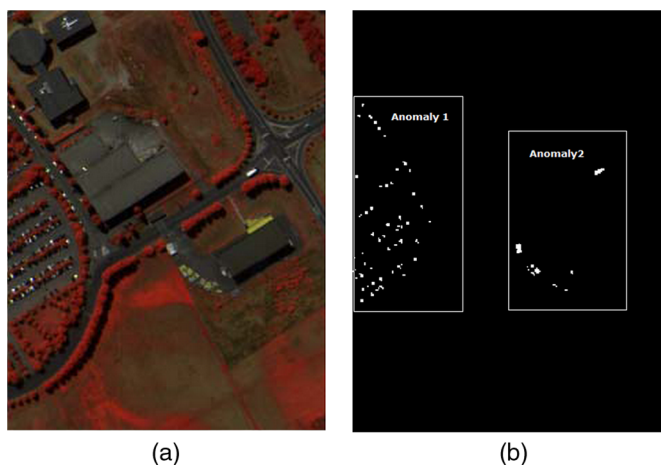


**Fig. 4** (a) The false-color image (bands 80, 70, and 30) and (b) the ground truth of anomalies in PaviaU dataset.

$k$ -means algorithm. The Gaussian RBF kernel is used in the LSVDD detector and the parameter  $\sigma$  is determined by implementing the approximate minimum-maximum approach on randomly selected 10 regions of the image to represent the background.

### 3.2.1 Separability performance of LRaSMD detector

The experiment analyzes the ability of the new detector to distinguish anomalies from the background. To make a holistic analysis, we compare the detection results of LRaSMD with three other widely used detectors, including GRX, OSP-GRX, and CB. The detailed parameter configurations of all four detectors on three HSI datasets are shown in Table 3. For the PaviaC dataset, the rank  $r$  of the background matrix and the sparsity level  $k$  of the anomaly matrix in LRaSMD detector are set to be 2 and 0.45, respectively, using cross-validation; the number of clusters  $C$  in CB detector is manually set to be 3, the same number as the number of main ground objects; the projected dimension  $P$  in the OSP-GRX is set to be 8 after cross-validation. For the Botswana dataset, after cross-validation, the background rank  $r$  and the sparsity level  $k$  in LRaSMD detector are set to be 4 and 0.4, respectively;  $C$  in the CB detector is manually set to be 4, the same number as the number of main ground objects;  $P$  in the OSP-GRX is set to be 5 after cross-validation. For the PaviaU dataset,  $r$  and  $k$  in LRaSMD are set to be 5 and 0.45, respectively, using cross-validation;  $C$  in the CB is manually set to be 6 and  $P$  in the OSP-GRX is set to be 4 using cross-validation.

Figure 5 shows the three-dimensional plots of detection results from all four detectors on the three HSI datasets without thresholding. We observe that the LRaSMD detector keeps the background pixels into a small range of values while augmenting the anomalies. The anomaly pixels then perfectly separate from the background and obviously stand out in the image scene. Compared with LRaSMD, the GRX, OSP-GRX, and CB detectors output the background pixels with some fluctuations, and hence, the separability between anomalies and background degrades. Through the orthogonal subspace projection, the OSP-GRX detector performs better than GRX and outputs the background pixels within a smaller and smoother range. In most cases, the results from CB detector are the worst among all four detectors, with the background containing the most fluctuations. From the above observations, we summarize that the

**Table 3** The parameter settings of all experiments on the PaviaC, Botswana, and PaviaU datasets (the symbol “—” means no parameter involved in the detector).

Experiments	Detectors	Datasets		
		PaviaC	Botswana	PaviaU
Experiment 1	LRaSMD	$r = 2; k = 0.45$	$r = 4; k = 0.4$	$r = 5; k = 0.45$
	GRX	—	—	—
	OSP-GRX	$P = 8$	$P = 5$	$P = 4$
	CB	$C = 3$	$C = 4$	$C = 6$
Experiment 2	LRaSMD	$r = 2$ to $10; k = 0.45$	$r = 2$ to $10; k = 0.4$	$r = 2$ to $10; k = 0.45$
Experiment 3	LRaSMD	$r = 2; k = 0.05$ to $0.65$	$r = 4; k = 0.15$ to $0.55$	$r = 7; k = 0.10$ to $0.70$
Experiment 4	LRaSMD	$r = 2; k = 0.47$	$r = 4; k = 0.4$	$r = 5; k = 0.45$
	GRX	—	—	—
	OSP-GRX	$P = 8$	$P = 5$	$P = 4$
	CB	$C = 3$	$C = 4$	$C = 6$
LSVDD		$w_i = 7 \times 7;$ $w_o = 17 \times 17;$ $\sigma = 8$	$w_i = 5 \times 5;$ $w_o = 15 \times 15;$ $\sigma = 7$	$w_i = 11 \times 11;$ $w_o = 21 \times 21;$ $\sigma = 12$

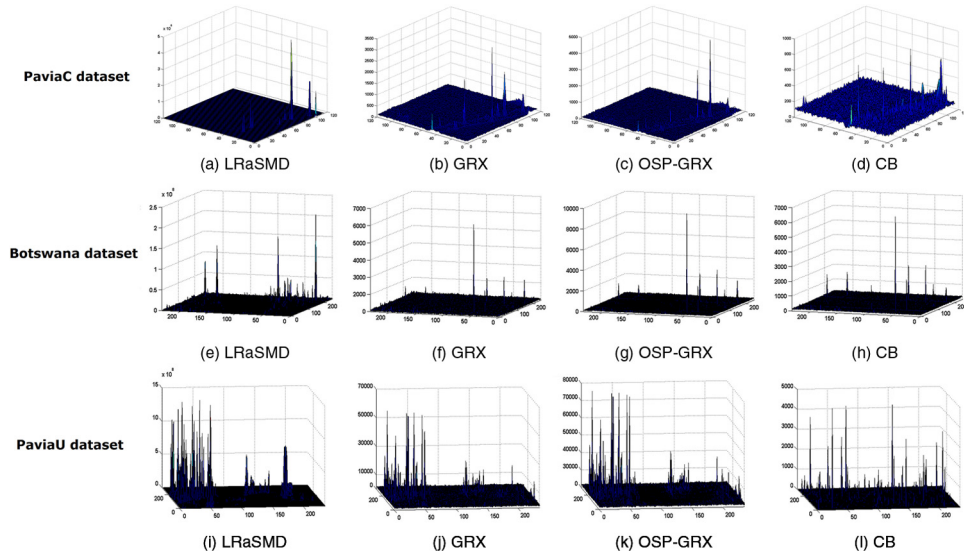


**Fig. 5** The plots of three-dimension detection results on the three datasets without thresholding.

separability performance of the LRaSMD detector is better than those of the GRX, OSP-GRX, and CB detectors.

### 3.2.2 Effects from the rank of background matrix

This experiment investigates the performance sensitivity of LRaSMD with respect to the rank parameter of the background matrix. In the experiment, the rank of background matrix in LRaSMD on all three datasets is manually set between 2 and 10 with a step interval of 2. Using cross-validation, the sparsity levels of the PaviaC and PaviaU dataset are set to be 0.45 and the sparsity level of the Botswana dataset is set to be 0.4. The detailed parameter information of the LRaSMD detector on all three detectors is listed in Table 3.

Figure 6 shows the results of ROC curves from LRaSMD detector on all three detectors with the changing background rank  $r$  between 2 and 10. For the PaviaC dataset in Fig. 6(a), the LRaSMD detector performs best when the rank  $r$  of the background equals 2. With  $r$  increasing from 2 to 10, the detection performance of LRaSMD gradually decreases, and the ROC curve of background rank at 10 has the highest false alarm rate when achieving the 100% probability of detection. For the Botswana dataset in Fig. 6(b), the detection performance of LRaSMD detector improves as the background rank  $r$  increases from 2 to 4. The ROC curve result is best when the background rank  $r$  equals 4. After that, with  $r$  continuously increasing from 4 to 10, the detection performance of LRaSMD begins to decrease. The ROC curve of the background rank at 10 performs the worst among all the curves, having the highest false alarm rate at 100% probability of detection. For the PaviaU dataset in Fig. 6(c), the detection performance of LRaSMD increases as the background matrix rises from 2 to 6. The LRaSMD achieves the best performance when  $r$  equals 6. After that, the detection performance of LRaSMD degrades as the background rank  $r$  increases from 6 to 10.

We summarize the following from the above three observations. First, the detection performance of the LRaSMD detector is sensitive to the background rank  $r$ . Second, a too-small or too-large rank will significantly affect the detection performance of the detector. The reason for that is as follows. A too-small background rank makes the background matrix in LRaSMD lack the capability to capture the variability of the spectral information in HSI data and, therefore, negatively affects the detection performance of the new detector. In contrast, if the rank is too large, the background takes too much of the spectral information from the HSI data, and some spectral features that should have been labeled anomalies would be included in the background matrix. This also decreases the separability between anomalies and background when using the anomaly matrix. In this situation, the detection performance degrades and the false alarm rate increases if we want a 100% probability of detection. Moreover, we make intercomparisons between the

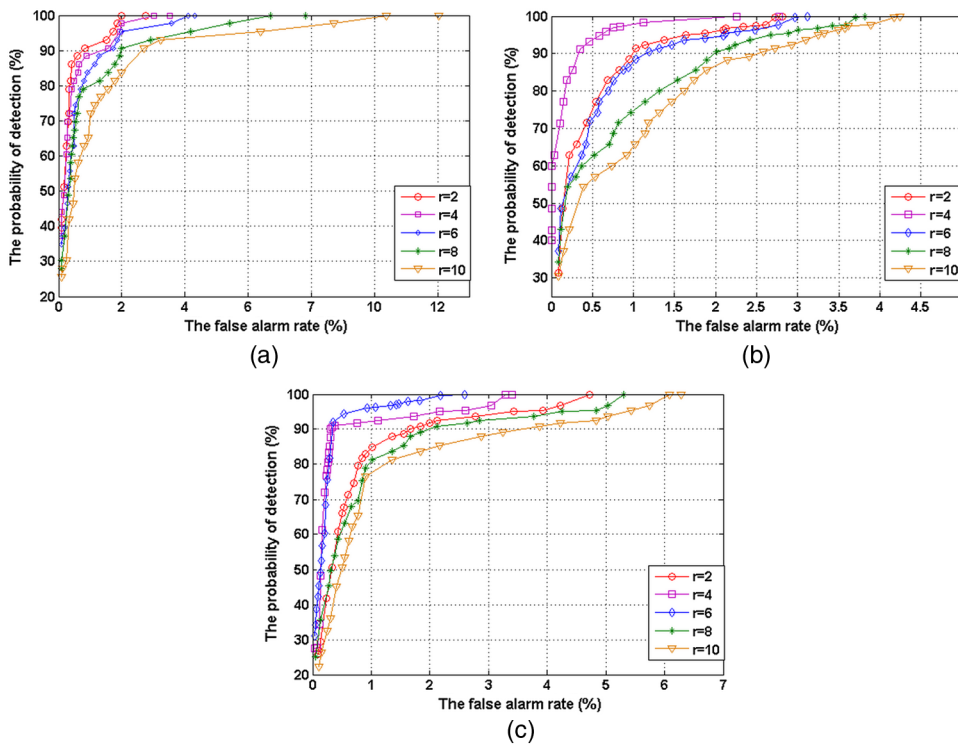


**Fig. 6** The receiver operating characteristic (ROC) curves of low-rank and sparse matrix decomposition (LRaSMD) detector with the changing background rank on the (a) PaviaC, (b) Botswana, and (c) PaviaU datasets.

number of main ground objects in the three HSI datasets and the proper background rank at which the LRaSMD has the best detection performance. We found that the proper background rank monotonically increases with the number of ground objects in the HSI dataset. A larger class number characterizes larger diversity in spectral information of main ground objects in HSI data and, therefore, requires a higher rank of background to capture the variability of the spectral information. The proper background rank for each dataset almost equals its number of main ground objects in the image scene.

### 3.2.3 Effects from the sparsity level of anomaly matrix

The experiment analyzes the performance sensitivity of LRaSMD with respect to the sparsity level of the anomaly matrix. For the PaviaC dataset, the sparsity level  $k$  of the anomaly matrix is manually set between 0.05 and 0.65 with a step interval of 0.15, and the background rank  $r$  is set to be 2 using cross-validation. For the Botswana dataset, the sparsity level  $k$  of the anomaly matrix is manually set between 0.15 and 0.55 with a step interval of 0.1, and the background rank  $r$  is set to be 4 after cross-validation. For the PaviaU dataset, the sparsity level  $k$  of the anomaly matrix is manually set between 0.10 and 0.70 with a step interval of 0.15, and the background rank  $r$  is set to be 7 using cross-validation. Table 3 lists the detailed parameter information of the LRaSMD detector on all three datasets.

Figure 7 shows the ROC curves of the LRaSMD detector with the changing sparsity level  $k$  of the anomaly matrix on the three datasets. For the PaviaC dataset in Fig. 7(a), the LRaSMD performs worst when the sparsity level  $k$  of the anomaly matrix equals 0.05. The detection performance of LRaSMD improves as the sparsity level  $k$  increases from 0.05 to 0.50 and achieves the best when  $k$  equals 0.50. After that, the performance of LRaSMD decreases when the  $k$  continuously increases from 0.50 to 0.65. For the Botswana dataset in Fig. 7(b), the performance of LRaSMD first increases as the sparsity level  $k$  rises from 0.15 to 0.35 and then gradually decreases when  $k$  is between 0.35 and 0.55. The LRaSMD detector performs worst when  $k$  equals 0.55 and has the highest false alarm rate at 100% probability of detection. Similarly,

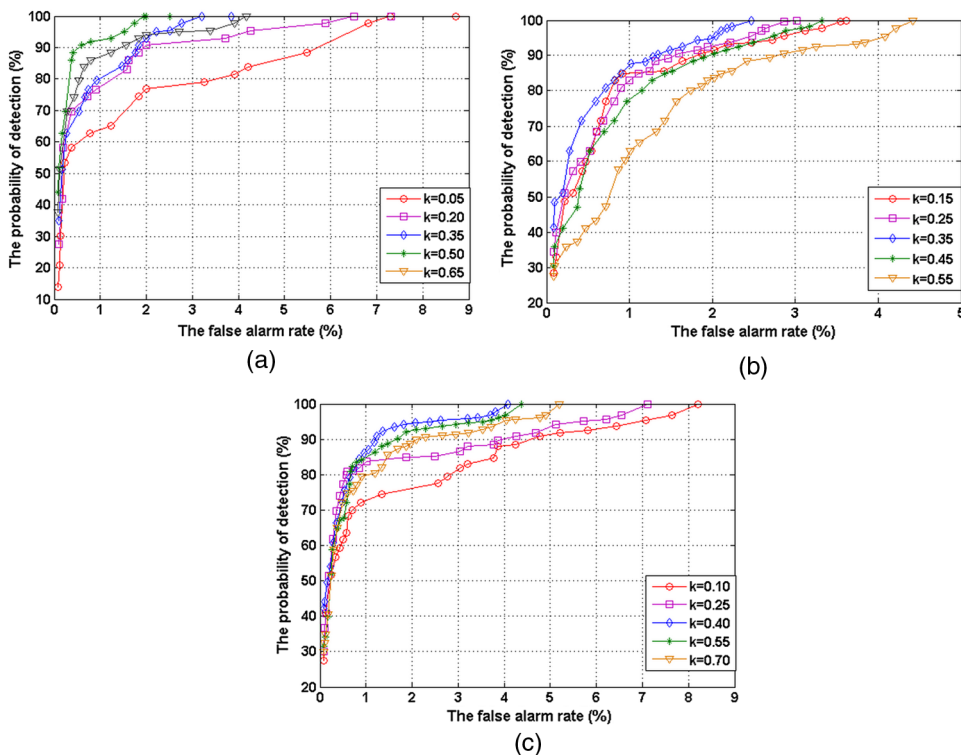


**Fig. 7** The ROC curves of LRaSMD detector with the changing sparsity level of the anomaly matrix on the (a) PaviaC, (b) Botswana, and (c) PaviaU datasets.

the LRaSMD on the PaviaU dataset achieves the best performance when the sparsity level  $k$  equals 0.40, and a sparsity level  $k$  either smaller or larger than 0.4 makes the detection performance of LRaSMD decrease.

We make some summarizations from the above three observations. First, the detection performance of the LRaSMD detector is sensitive to the sparsity level  $k$  of the anomaly matrix. Second, the detection performance of LRaSMD initially increases as the sparsity level  $k$  increases from a smaller value, achieves the best performance at the proper sparsity level value, and then gradually decreases as  $k$  continuously increases. A too-small or too-large sparsity level results in a decrease in the detection performance of the LRaSMD. The explanation for that is as follows. Increasing the sparsity level  $k$  from a smaller value includes more and more distinctive features of the anomalies into the anomaly matrix and, therefore, promotes the detection performance of the LRaSMD. However, with the continual increase of the sparsity level, some spectral features of background pixels are also included into the anomaly matrix. That reduces the distinguishing ability of the anomaly matrix and, therefore, degrades the detection performance of the new detector. Moreover, we make comparisons between the true ratios of anomaly pixels in the three datasets with the proper sparsity levels at which the LRaSMD detector performs best. We found that for each dataset, the proper sparsity level  $r$  significantly exceeds the true ratio of anomalies in the image scene.

### 3.2.4 Detection performance of LRaSMD detector

The experiment explores the detection performance of the LRaSMD detector. We make holistic comparisons in the ROC curves between the LRaSMD detector and other four state-of-the-art detectors: GRX, OSP-GRX, CB, and LSVDD. In the experiment, for the PaviaC dataset, using cross-validation, the rank  $r$  of the background matrix and the sparsity level  $k$  of the anomaly matrix in LRaSMD detector are set to be 2 and 0.47, respectively. The number of clusters  $C$  in CB detector is manually set to be 3; the projected dimension  $P$  in the OSP-GRX is set to be 8 after cross-validation; the dimensions of the inner region  $w_i$  and outer region  $w_o$  for the hollow background window in LSVDD are manually selected to be  $7 \times 7$  and  $17 \times 17$ , respectively, and

the parameter  $\sigma$  is set to be 8 by using the approximate minimum-maximum approach. For the Botswana dataset, determined by cross-validation, the background rank  $r$  and the sparsity level  $k$  in LRaSMD detector are set to be 4 and 0.4, respectively;  $C$  in the CB detector is manually set to be 4;  $P$  in the OSP-GRX is set to be 5 using cross-validation; the dimensions of  $w_i$  and  $w_o$  in LSVDD are manually set to be  $5 \times 5$  and  $15 \times 15$ , respectively, and the parameter  $\sigma$  is set to be 7. For the PaviaU dataset,  $r$  and  $k$  in LRaSMD are set to be 5 and 0.45, respectively, using cross-validation;  $C$  in the CB is manually set to be 6 and  $P$  in the OSP-GRX is set to be 4 using cross-validation; the dimensions of  $w_i$  and  $w_o$  in LSVDD are manually selected to be  $11 \times 11$  and  $21 \times 21$ , and the parameter  $\sigma$  is set to be 12. Table 3 lists the detailed parameter information of all five detectors on three HSI datasets in the experiment.

Figure 8 shows the results of ROC curves from all five detectors on the three HSI datasets. For the PaviaC dataset of Fig. 8(a), LRaSMD outperforms GRX, OSP-GRX, and CB throughout the curve. Moreover, LRaSMD generates slightly better detection performance than LSVDD, having only  $\sim 2\%$  probability of false alarm rate when achieving 100% probability of detection. OSP-GRX performs better than GRX and CB, but slightly worse than LSVDD. The ROC curve of CB detector is the worst among all five detectors. For the Botswana dataset of Fig. 8(b), throughout the whole curve, LRaSMD performs best among all five detectors, having 2.17% probability of false alarm rate when achieving 100% probability of detection. OSP-GRX detector outperforms GRX and CB detectors, but behaves worse than LSVDD detector. The ROC curve of GRX has the highest false alarm rate among all five detectors, with 7.6% false alarm rate when achieving 100% probability of detection. For the PaviaU dataset of Fig. 8(c), LRaSMD detector outperforms GRX, OSP-GRX, and CB throughout the curve. LRaSMD detector achieves a higher probability of detection than LSVDD when the false alarm rate is  $< 1.54\%$ . After that, LRaSMD begins to perform worse than LSVDD, and its false alarm rate is slightly higher than LSVDD when achieving 100% probability of detection. The OSP-GRX detector still outperforms the GRX detector, having a lower false alarm rate at 100% probability of detection. The CB detector performs the worst, with the highest false alarm rate when achieving 100% probability of detection.

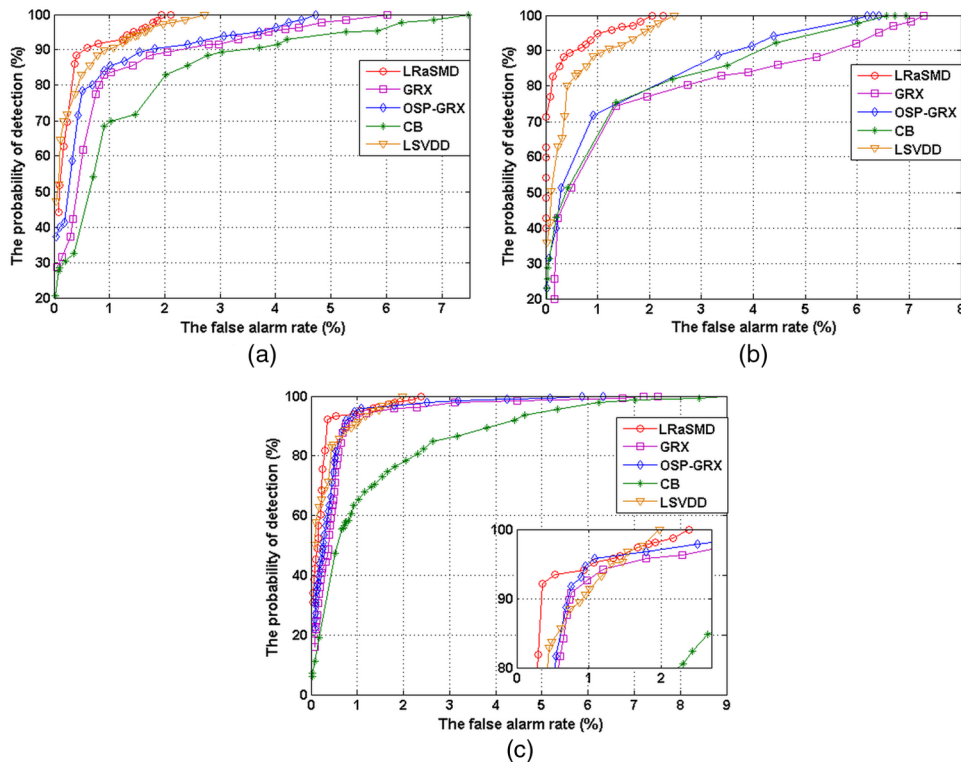


**Fig. 8** The ROC curves of LRaSMD and other four detectors on the (a) PaviaC, (b) Botswana, and (c) PaviaU datasets.

**Table 4** The contrast in computational time between LRaSMD, GRX, OSP-GRX, CB, and LSVDD detectors.

Datasets	Computational time of detectors (seconds)				
	LRaSMD	GRX	OSP-GRX	CB	LSVDD
PaviaC	32.4	18.2	148.2	44.2	62.6
Botswana	103.3	67.1	558.2	160.8	210.4
PaviaU	83.6	48.1	377.9	120.5	197.7

Moreover, Table 4 compares the computational times of all five detectors. The codes for all the methods were implemented in MATLAB® 2010b and run on a Dell Computer with Xeon E5400 2.83 GHz processor and 32 GB of RAM on a Windows 7 operating system. From the table, we observe the computational time of LRaSMD is longer than the GRX computational time, but is shorter than the computational times of OSP-GRX, CB, and LSVDD detectors.

We summarize the results from the above observations. First, LRaSMD detector performs better than GRX, OSP-GRX, and CB detectors. Second, LRaSMD detector provides detection performance equal to or better than LSVDD. Third, OSP-GRX performs better than GRX and CB detectors, whereas it is worse than LSVDD. Finally, LRaSMD detector has the second shortest computational time among all five detectors.

### 3.3 Discussions

The above four groups of experiments on the three HSI datasets completely analyze the separability and detection performances of LRaSMD detector. Compared with GRX, OSP-GRX, and CB detectors, LRaSMD detector has the best separability performance in distinguishing the anomalies from the background. GRX, OSP-GRX, and CB detectors construct the background using clustering or statistical algorithms and then separate the anomalies from the background using spectral differences. In this situation, the background model includes anomalies that degrade the detection performance. In contrast, LRaSMD detector assumes anomalies are gross errors that deviate from the normal spectral measurements in each band. By reconstructing the sparse anomaly matrix and the low-rank background matrix in one step, the new detector separates the anomalies from the background in one step. This one step separation allows the LRaSMD detector to have better separability performance and to outperform the above three detectors in anomaly detection.

The comparisons in detection performance among five detectors (LRaSMD, GRX, OSP-GRX, CB, and LSVDD) also show that the LRaSMD provides an equal or better detection result than SVDD. The computational time of LRaSMD detector is shorter than those of OSP-GRX, CB, and LSVDD detectors but longer than that of GRX detector. The performance of LSVDD is better than GRX, OSP-GRX, and CB detectors. OSP-GRX detector distinguishes anomalies better than GRX and CB detectors because it suppresses the background using orthogonal projections. The performance of CB detector is relatively unstable, in part because it depends on the clustering results.

Moreover, the experiment on the effects from the background rank on the performance sensitivity of LRaSMD shows that a too-small or too-large background rank would degrade the detection performance of LRaSMD. Therefore, in realistic application, a moderate low background rank is more suitable for the HSI dataset. In addition, the sparsity level of the anomaly matrix is also sensitive to the detection performance of LRaSMD. A too-small or too-large sparsity level would decrease the performance of LRaSMD and a moderate sparsity level is more suitable for the new detector in realistic anomaly detection applications.

## 4 Conclusions and Future Work

This paper proposes the LRaSMD method to detect anomalies in HSI data. The new method separates the anomaly information (i.e., the sparse matrix) from the background information

(i.e., the low-rank matrix) in one step. The separability and detection performances of the new detector are completely investigated using four groups of experiments on three realistic HSI datasets. First, the separation ability of the detector is tested and compared against the performance of GRX, OSP-GRX, and CB detectors. LRaSMD detector's separation ability exceeds those of the other three detectors. Second, the detection performance of the new LRaSMD detector is analyzed and compared against the detection performance of the other four state-of-the-art detectors: GRX, OSP-GRX, CB, and LSVDD. The results show that with the second shortest computational time among all five detectors, LRaSMD performs better than GRX, OSP-GRX, and CB detectors, and achieves better or equal detector performance than LSVDD. Finally, the effects from two main parameters, including the background rank and the sparsity level of the anomalies, on the performance sensitivity of LRaSMD are analyzed. A moderate low background rank in HSI data and a moderate sparsity level of the anomaly matrix guarantee better detection performance of the LRaSMD detector. In future work, we will utilize more realistic HSI datasets to quantitatively study the relationships between the background rank  $r$  and the number of classes in HSI data. We will also investigate ways to improve the speed of the LRaSMD method to make it a feasible algorithm for real-time applications. Moreover, we will study how to adaptively set the threshold parameter  $\eta$  to make the LRaSMD detector more feasible for practical applications in anomaly detection. In addition, we will further compare the LRaSMD detector against other popular detectors, including maximum orthogonal complement analysis (MOCA)<sup>50</sup> and modified MOCA (Ref. 51), on more realistic HSI datasets to further testify our proposed detectors.

## Acknowledgments

This work was funded by “973” National Basic Research Program of China (2013CB733204) in Tongji University, Shanghai, and sponsored by K. C. Wong Magna Fund in Ningbo University, Zhejiang, China. The authors thank Rongrong Wang of the Norbert Wiener Center for the helpful suggestions. The authors would also like to thank the editor and referees for their suggestions, which improved the manuscript.

## References

1. D. Landgrebe, “Hyperspectral image data analysis,” *IEEE Signal Process. Mag.* **19**(1), 17–28 (2002), <http://dx.doi.org/10.1109/79.974718>.
2. M. Liu et al., “Wavelet-based detection of crop zinc stress assessment using hyperspectral reflectance,” *Comput. Geosci.* **37**(9), 1254–1263 (2011), <http://dx.doi.org/10.1016/j.cageo.2010.11.019>.
3. M. Prabhakar et al., “Use of ground based hyperspectral remote sensing for detection of stress in cotton caused by leafhopper (Hemiptera: Cicadellidae),” *Comput. Electron. Agric.* **79**(2), 189–198 (2011), <http://dx.doi.org/10.1016/j.compag.2011.09.012>.
4. A. Brook and E. Ben-Dor, “Quantitative detection of sediment dust analog over green canopy using airborne hyperspectral imagery,” in *2nd Workshop on Hyperspectral Image and Signal Processing: Evolution in Remote Sensing*, pp. 1–5 (2010).
5. A. Chudnovsky et al., “Hyperspectral spaceborne imaging of dust-laden flows: anatomy of Saharan dust storm from the Bodélé Depression,” *Remote Sens. Environ.* **115**(4), 1013–1024 (2011), <http://dx.doi.org/10.1016/j.rse.2010.12.006>.
6. M. E. Andrew and S. L. Ustin, “The role of environmental context in mapping invasive plants with hyperspectral image data,” *Remote Sens. Environ.* **112**(12), 4301–4317 (2008), <http://dx.doi.org/10.1016/j.rse.2008.07.016>.
7. X. Miao et al., “Detection and classification of invasive saltcedar through high spatial resolution airborne hyperspectral imagery,” *Int. J. Remote Sens.* **32**(8), 2131–2150 (2011), <http://dx.doi.org/10.1080/01431161003674618>.
8. P. W. T. Yuen and M. Richardson, “An introduction to hyperspectral imaging and its application for security, surveillance and target acquisition,” *Imaging Sci. J.* **58**(5), 241–253 (2010), <http://dx.doi.org/10.1179/174313110X12771950995716>.

9. K. Tiwari, M. Arora, and D. Singh, "An assessment of independent component analysis for detection of military targets from hyperspectral images," *Int. J. Appl. Earth Obs. Geoinf.* **13**(5), 730–740 (2011), <http://dx.doi.org/10.1016/j.jag.2011.03.007>.
10. A. Banerjee, P. Burlina, and C. Diehl, "A support vector method for anomaly detection in hyperspectral imagery," *IEEE Trans. Geosci. Remote Sens.* **44**(8), 2282–2291 (2006), <http://dx.doi.org/10.1109/TGRS.2006.873019>.
11. S. Khazai et al., "Anomaly detection in hyperspectral images based on an adaptive support vector method," *IEEE Geosci. Remote Sens. Lett.* **8**(4), 646–650 (2011), <http://dx.doi.org/10.1109/LGRS.2010.2098842>.
12. C. I. Chang, *Hyperspectral Imaging: Techniques for Spectral Detection and Classification*, Springer-Verlag, New York (2003).
13. H. Kwon and N. M. Nasrabadi, "Kernel RX-algorithm: a nonlinear anomaly detector for hyperspectral imagery," *IEEE Trans. Geosci. Remote Sens.* **43**(2), 388–397 (2005), <http://dx.doi.org/10.1109/TGRS.2004.841487>.
14. C. I. Chang and S. S. Chiang, "Anomaly detection and classification for hyperspectral imagery," *IEEE Trans. Geosci. Remote Sens.* **40**(6), 1314–1325 (2002), <http://dx.doi.org/10.1109/TGRS.2002.800280>.
15. D. W. J. Stein et al., "Anomaly detection from hyperspectral imagery," *IEEE Signal Process. Mag.* **19**(1), 58–69 (2002), <http://dx.doi.org/10.1109/79.974730>.
16. I. S. Reed and X. Yu, "Adaptive multiple-band CFAR detection of an optical pattern with unknown spectral distribution," *IEEE Trans. Acoust., Speech Signal Process.* **38**(10), 1760–1770 (1990), <http://dx.doi.org/10.1109/29.60107>.
17. N. Henze and T. Wagner, "A new approach to the BHEP tests for multivariate normality," *J. Multivar. Anal.* **62**(1), 1–23 (1997), <http://dx.doi.org/10.1006/jmva.1997.1684>.
18. M. J. Carlotto, "A cluster-based approach for detecting man-made objects and changes in imagery," *IEEE Trans. Geosci. Remote Sens.* **43**(2), 374–387 (2005), <http://dx.doi.org/10.1109/TGRS.2004.841481>.
19. P. Bajorski, "Practical evaluation of max-type detectors for hyperspectral images," *IEEE J. Sel. Topics Appl. Earth Obs. Remote Sens.* **5**(2), 462–469 (2012), <http://dx.doi.org/10.1109/JSTARS.2012.2188278>.
20. C. I. Chang, "Orthogonal subspace projection (OSP) revisited: a comprehensive study and analysis," *IEEE Trans. Geosci. Remote Sens.* **43**(3), 502–518 (2005), <http://dx.doi.org/10.1109/TGRS.2004.839543>.
21. P. Bajorski, "Target detection under misspecified models in hyperspectral images," *IEEE J. Sel. Topics Appl. Earth Obs. Remote Sens.* **5**(2), 470–477 (2012), <http://dx.doi.org/10.1109/JSTARS.2012.2188095>.
22. K. I. Ranney and M. Soumekh, "Hyperspectral anomaly detection within the signal subspace," *IEEE Geosci. Remote Sens. Lett.* **3**(3), 312–316 (2006), <http://dx.doi.org/10.1109/LGRS.2006.870833>.
23. P. Gurram, H. Kwon, and T. Han, "Sparse kernel-based hyperspectral anomaly detection," *IEEE Geosci. Remote Sens. Lett.* **9**(5), 943–947 (2012), <http://dx.doi.org/10.1109/LGRS.2012.2187040>.
24. J. A. Malpica, J. G. Rejas, and M. C. Alonso, "A projection pursuit algorithm for anomaly detection in hyperspectral imagery," *Pattern Recognit.* **41**(11), 3313–3327 (2008), <http://dx.doi.org/10.1016/j.patcog.2008.04.014>.
25. T. E. Smetek and K. W. Bauer, "A comparison of multivariate outlier detection methods for finding hyperspectral anomalies," *Mil. Oper. Res.* **13**(4), 19–43 (2008), <http://dx.doi.org/10.5711/morj.13.4.19>.
26. S. Matteoli, M. Diani, and G. Corsini, "A tutorial overview of anomaly detection in hyperspectral images," *IEEE Aerosp. Electron. Syst. Mag.* **25**(7), 5–28 (2010), <http://dx.doi.org/10.1109/MAES.2010.5546306>.
27. L. Ma, M. M. Crawford, and J. Tian, "Anomaly detection for hyperspectral images based on robust locally linear embedding," *J. Infrared Millim. Terahertz Waves* **31**(6), 753–762 (2010), <http://dx.doi.org/10.1007/s10762-010-9630-3>.

28. L. Ma, M. M. Crawford, and J. Tian, "Anomaly detection for hyperspectral images using local tangent space alignment," in *IEEE Int. Geoscience and Remote Sensing Symp.*, pp. 824–827 (2010).
29. L. Xiong, X. Chen, and J. Schneider, "Direct robust matrix factorization for anomaly detection: data mining (ICDM)," in *IEEE 11th Int. Conf. on Data Mining (ICDM)*, pp. 844–853 (2011).
30. M. Golbabae and P. Vandergheynst, "Hyperspectral image compressed sensing via low-rank and joint-sparse matrix recovery," in *IEEE Int. Conf. on Acoustics, Speech and Signal Processing (ICASSP)*, pp. 2741–2744 (2012).
31. K. Rong et al., "Low-rank and sparse matrix decomposition-based pan sharpening," in *IEEE Int. Geoscience and Remote Sensing Symp. (IGARSS)*, pp. 2276–2279 (2012).
32. X. Zhang et al., "SAR image change detection based on low rank matrix decomposition," in *IEEE Int. Geosci. Remote Sensing Symp. (IGARSS)*, pp. 6271–6274 (2012).
33. C. I. Chang and D. C. Heinz, "Constrained subpixel target detection for remotely sensed imagery," *IEEE Trans. Geosci. Remote Sens.* **38**(3), 1144–1159 (2000), <http://dx.doi.org/10.1109/36.843007>.
34. E. J. Candès et al., "Robust principal component analysis?," *J. ACM* **58**(3), 1027–1063 (2009), <http://dx.doi.org/10.1145/1970392.1970395>.
35. A. Ifarraguerri and C. I. Chang, "Unsupervised hyperspectral image analysis with projection pursuit," *IEEE Trans. Geosci. Remote Sens.* **38**(6), 2529–2538 (2000), <http://dx.doi.org/10.1109/36.885200>.
36. J. M. Bioucas-Dias and J. M. P. Nascimento, "Hyperspectral subspace identification," *IEEE Trans. Geosci. Remote Sens.* **46**(8), 2435–2445 (2008), <http://dx.doi.org/10.1109/TGRS.2008.918089>.
37. Z. Lin et al., "Fast convex optimization algorithms for exact recovery of a corrupted low-rank matrix," in *3rd IEEE Int. Workshop on Computational Advances in Multi-Sensor Adaptive Processing (CAMSAP)*, pp. 213–216 (2009).
38. Z. Zhou et al., "Stable principal component pursuit," in *IEEE Int. Symp. on Information Theory Proceedings (ISIT)*, pp. 1518–1522 (2010).
39. T. Zhou and D. Tao, "Godec: randomized low-rank & sparse matrix decomposition in noisy case," in *28th Int. Conf. on Machine Learning (ICML)*, pp. 33–40 (2011).
40. K. Bredies and D. A. Lorenz, "Iterated hard shrinkage for minimization problems with sparsity constraints," *SIAM J. Sci. Comput.* **30**(2), 657–683 (2008), <http://dx.doi.org/10.1137/060663556>.
41. M. Fazel et al., "Compressed sensing and robust recovery of low rank matrices," in *42nd Asilomar Conf. on Signals, Systems and Computers*, pp. 1043–1047 (2008).
42. S. Roweis, "EM algorithms for PCA and SPCA," in *Proc. of Conf. on Advances in Neural Information Processing Systems*, pp. 626–632 (1998).
43. J. M. Bioucas-Dias and J. M. P. Nascimento, "Estimation of signal subspace on hyperspectral data," *Proc. SPIE* **5982**, 59820L (2005), <http://dx.doi.org/10.1117/12.620061>.
44. O. Duran and M. Petrou, "A time-efficient method for anomaly detection in hyperspectral images," *IEEE Trans. on Geosci. Remote Sens.* **45**(12), 3894–3904 (2007), <http://dx.doi.org/10.1109/TGRS.2007.909205>.
45. A. Plaza et al., "Dimensionality reduction and classification of hyperspectral image data using sequences of extended morphological transformations," *IEEE Trans. Geosci. Remote Sens.* **43**(3), 466–479 (2005), <http://dx.doi.org/10.1109/TGRS.2004.841417>.
46. M. Fauvel et al., "Spectral and spatial classification of hyperspectral data using SVMs and morphological profiles," *IEEE Trans. Geosci. Remote Sens.* **46**(11), 3804–3814 (2008), <http://dx.doi.org/10.1109/TGRS.2008.922034>.
47. W. Liao et al., "Classification of hyperspectral data over urban areas using directional morphological profiles and semi-supervised feature extraction," *IEEE J. Sel. Topics Appl. Earth Obs. Remote Sens.* **5**(4), 1177–1190 (2012), <http://dx.doi.org/10.1109/JSTARS.2012.2190045>.
48. J. Ham et al., "Investigation of the random forest framework for classification of hyperspectral data," *IEEE Trans. Geosci. Remote Sens.* **43**(3), 492–501 (2005), <http://dx.doi.org/10.1109/TGRS.2004.842481>.

49. L. Ma, M. M. Crawford, and J. Tian, "Local manifold learning-based k-nearest-neighbor for hyperspectral image classification," *IEEE Trans. Geosci. Remote Sens.* **48**(11), 4099–4109 (2010), <http://dx.doi.org/10.1109/TGRS.2010.2055876>.
50. O. Kuybeda, D. Malah, and M. Barzohar, "Rank estimation and redundancy reduction of high-dimensional noisy signals with preservation of rare vectors," *IEEE Trans. Signal Process.* **55**(12), 5579–5592 (2007), <http://dx.doi.org/10.1109/TSP.2007.901645>.
51. N. Acito, M. Diani, and G. Corsini, "Hyperspectral signal subspace identification in the presence of rare signal components," *IEEE Trans. Geosci. Remote Sens.* **48**(4), 1940–1954 (2010), <http://dx.doi.org/10.1109/TGRS.2009.2035445>.

**Weiwei Sun** is an assistant professor at Ningbo University, Zhejiang Province, China. He received his BS degree in surveying and mapping from Tongji University in 2007 and his PhD degree in cartography and geographic information engineering from Tongji University in 2013. He has published more than 20 journal papers and his current research interests include hyperspectral image processing with manifold learning and anomaly detection of remote sensing imagery using compressive sensing.

Biographies of the other authors are not available.